

# **Supplementary material – In-depth characterisation of organic matter lability and composition from Arctic Permafrost thaw slumps**

Marco A. Bolandini<sup>1</sup>, Negar Haghipour<sup>1,2</sup>, Kirsi H. Keskitalo<sup>4</sup>, Jorien E. Vonk<sup>3</sup>, Jordon D. Hemingway<sup>1</sup>, Timothy I. Eglinton<sup>1</sup>, Lisa Bröder<sup>1</sup>

5 <sup>1</sup>Geological Institute, Department of Earth and Planetary Sciences, ETH Zurich, Sonneggstrasse 5, 8092 Zurich, Switzerland

<sup>2</sup>Laboratory for Ion Beam Physics, Department of Physics, ETH Zurich, Otto-Stern-Weg 5, 8093 Zurich, Switzerland

<sup>3</sup>Earth and Climate, Faculty of Science, Vrije Universiteit Amsterdam, De Boelelaan 1085, 1081 HV Amsterdam, Netherlands

<sup>4</sup>School of Geography and Natural Sciences, Northumbria University, Ellison Place, Newcastle upon Tyne UK-NE1 8ST, United Kingdom

10 *Correspondence to:* Marco A. Bolandini (marcobo@caps.ethz.ch)

**Supplementary material**

Supplementary tables

**Table S1.** Summary of integrated thermal stability and radiocarbon parameters for each sample. Columns show: sample name, maximum activation energy ( $E_{\text{max}}$ , kJ mol<sup>-1</sup>), mean activation energy ( $E_{\text{mean}}$ , kJ mol<sup>-1</sup>) with standard deviation ( $\pm$  kJ mol<sup>-1</sup>), maximum probability density  $p_0(E)$ , residual oxidisable carbon to total organic carbon ratio (ROC/TOC, %), threshold temperature for ROC/TOC (°C), estimated mass of ROC carbon ( $\mu\text{g}$ ), weighted fraction modern radiocarbon ( $F^{14}\text{C}$ ) with standard deviation ( $\pm$ ), total carbon mass ( $\mu\text{g}$ ), and associated mass error ( $\pm \mu\text{g}$ ).

Sample Name	E_max (kJ/mol)	E_mean (kJ/mol)	E_std (kJ/mol)	p0(E)_max	ROC/TOC (%)	Threshold ROC/TOC Temperature (°C)	Estimated ROC Carbon ( $\mu\text{g}$ )	Weighted $F^{14}\text{C}$	$F^{14}\text{C}$ std ( $\pm$ )	Total Carbon Mass ( $\mu\text{g}$ )	Total Mass Error ( $\pm \mu\text{g}$ )
Fm2_AL	158.271	151.802	17.086	0.027	4.300	477.000	53.877	0.704	0.009	1252.964	31.716
Fm2_HO1	156.015	165.165	20.700	0.022	33.100	441.100	155.063	0.120	0.007	468.467	11.858
Fm2_HO2	160.526	161.850	17.133	0.029	31.900	417.900	197.858	0.072	0.006	620.243	15.700
Fm2_PL	152.256	162.963	19.731	0.022	38.200	413.300	261.191	0.021	0.005	683.745	17.308
Fm2_RU	156.767	166.908	19.913	0.019	40.300	429.200	214.926	0.115	0.007	533.314	13.500
Fm3_AL2	172.556	151.955	21.151	0.021	14.600	451.600	148.104	0.333	0.008	1014.414	25.678
Fm3_AL3	140.226	155.535	23.718	0.017	31.700	406.000	167.240	0.282	0.008	527.571	13.354
Fm3_HO	162.030	170.921	24.275	0.019	36.400	438.700	203.082	0.036	0.005	557.917	14.123
Fm3_DB	160.526	168.637	22.510	0.020	38.700	428.500	189.067	0.039	0.005	488.546	12.367
Fm3_RU	156.767	166.908	19.913	0.019	35.600	419.000	227.568	0.049	0.005	639.237	16.181

20 **Table S2.** Bulk carbon composition of each sample. Columns show sample name, total sample weight (mg), total carbon content (TC, %), total organic carbon (TOC, %), total inorganic carbon released at 900 °C (TIC, %), organic carbon released at 400 °C (TOC<sub>400</sub>, %), and residual oxidisable carbon (ROC, %).

<b>Name</b>	<b>Weigh (mg)</b>	<b>TC (%)</b>	<b>TOC (%)</b>	<b>TIC (%)</b>
Fm2 AL	31.500	16.646	16.297	0.349
Fm2 HO1	79.700	1.143	1.028	0.115
Fm2 HO2	64.800	1.114	0.984	0.131
Fm2 PL	54.100	1.404	1.252	0.152
Fm2 RU	55.600	1.473	1.304	0.168
Fm3 AL2	40.300	7.575	7.276	0.299
Fm3 AL3	39.900	3.691	3.411	0.280
Fm3 HO	61.700	1.297	1.153	0.144
Fm3 DB	61.600	1.301	1.158	0.144
Fm3 RU	64.200	1.585	1.439	0.146
CB_AL1	40.200	1.857	1.646	0.210
CB_AL2	44.000	3.708	3.499	0.209
CB_AL3	45.700	2.700	2.500	0.200
CB_AL4	41.600	2.094	1.880	0.215
CB_HO	64.600	1.316	1.174	0.142
CB_DB	55.400	1.656	1.499	0.157
CB_RU	59.200	1.569	1.422	0.147
SF_AL	59.500	1.952	1.793	0.159
SF_HO	60.400	1.444	1.291	0.153
SF_DB	72.900	1.262	1.139	0.123
SF_RU	60.300	1.495	1.349	0.146

25 **Table S3.** Summary of ORO–AMS measurements for all samples and thermal windows. Columns show: sample ID, thermal window (°C), oxidation start time ( $t_0$ , s), oxidation end time ( $t_f$ , s), carbon mass released per thermal window ( $\mu\text{g}$ ) with associated uncertainty ( $\pm \mu\text{g}$ ), fraction modern radiocarbon ( $F^{14}\text{C}$ ) with standard deviation ( $\pm$ ), proportional contribution to total carbon release (fraction), mean activation energy ( $E$ ,  $\text{kJ mol}^{-1}$ ) with standard deviation ( $\pm \text{kJ mol}^{-1}$ ), and stable carbon isotope composition ( $\delta^{13}\text{C}$ , ‰).

Sample	Temperature Window (°C)	$t_0$ (s)	$t_f$ (s)	Mass thermal window ( $\mu\text{g}$ )	Mass error ( $\pm \mu\text{g}$ )	$F^{14}\text{C}$	$F^{14}\text{C}$ std ( $\pm$ )	fraction	E (kJ/mol)	E std. ( $\pm \text{kJ/mol}$ )
Fm2_AL	150-240	1385	2532	74.891	1.896	0.725	0.008	1	124	6
Fm2_AL	240-300	2533	3435	251.496	6.366	0.713	0.008	2	134	7
Fm2_AL	300-350	3436	4189	282.838	7.159	0.672	0.008	3	146	7
Fm2_AL	350-400	4190	4955	339.519	8.594	0.708	0.008	4	158	6
Fm2_AL	400-455	4956	5793	207.709	5.258	0.729	0.008	5	167	7
Fm2_AL	455-510	5794	6632	76.437	1.935	0.699	0.007	6	180	6
Fm2_AL	510-600	6633	8023	20.073	0.508	0.625	0.007	7	195	8
Fm2_AL	600-900	8024	10031	0.457	0.012	NA	NA	8	205	2
Fm2_HO1	150-240	1359	2508	5.074	0.128	0.262	0.005	1	130	6
Fm2_HO1	240-300	2509	3414	48.510	1.228	0.205	0.004	2	136	7
Fm2_HO1	300-350	3415	4179	88.143	2.231	0.139	0.003	3	147	7
Fm2_HO1	350-400	4180	4935	105.293	2.665	0.107	0.003	4	157	7
Fm2_HO1	400-455	4936	5772	84.113	2.129	0.096	0.003	5	171	9
Fm2_HO1	455-510	5773	6614	77.528	1.962	0.091	0.003	6	184	7
Fm2_HO1	510-600	6615	8009	59.805	1.514	0.102	0.004	7	197	7
Fm2_HO1	600-900	8010	9824	3.061	0.078	NA	NA	8	208	3
Fm2_HO2	150-240	1358	2485	4.287	0.109	0.209	0.005	1	132	6
Fm2_HO2	240-300	2486	3401	59.748	1.512	0.127	0.004	2	137	7
Fm2_HO2	300-350	3402	4154	119.813	3.033	0.079	0.003	3	148	7
Fm2_HO2	350-400	4155	4919	179.549	4.545	0.042	0.002	4	158	6
Fm2_HO2	400-455	4920	5758	137.144	3.472	0.052	0.002	5	168	7
Fm2_HO2	455-510	5759	6598	75.094	1.901	0.088	0.003	6	184	7
Fm2_HO2	510-600	6599	8007	44.609	1.129	0.123	0.004	7	194	6
Fm2_HO2	600-900	8008	10787	0.137	0.004	NA	NA	8	204	2
Fm2_PL	150-240	1468	2606	8.994	0.228	0.105	0.003	1	129	6
Fm2_PL	240-300	2607	3517	76.160	1.928	0.045	0.002	2	136	7
Fm2_PL	300-350	3518	4261	138.081	3.495	0.021	0.002	3	147	7
Fm2_PL	350-400	4262	5022	160.359	4.059	0.016	0.001	4	157	7
Fm2_PL	400-455	5023	5867	123.992	3.139	0.015	0.001	5	171	8
Fm2_PL	455-510	5868	6721	108.077	2.736	0.012	0.001	6	184	7
Fm2_PL	510-600	6722	8112	68.081	1.723	0.021	0.001	7	195	7
Fm2_PL	600-900	8113	10365	1.625	0.041	NA	NA	8	206	3
Fm2_RU	150-240	1472	2601	3.575	0.091	0.239	0.006	1	132	6
Fm2_RU	240-300	2602	3500	45.649	1.156	0.192	0.004	2	137	7
Fm2_RU	300-350	3501	4278	92.559	2.343	0.131	0.003	3	147	7
Fm2_RU	350-400	4279	5036	111.741	2.829	0.108	0.003	4	158	7
Fm2_RU	400-455	5037	5876	114.933	2.909	0.093	0.003	5	171	8
Fm2_RU	455-510	5877	6717	99.387	2.516	0.106	0.003	6	183	7
Fm2_RU	510-600	6718	8108	65.469	1.657	0.097	0.003	7	197	8
Fm2_RU	600-900	8109	10204	4.611	0.117	NA	NA	8	210	4



Sample	Temperature Window (°C)	t0 (s)	tf (s)	Mass thermal window (µg)	Mass error (± µg)	F <sup>14</sup> C	F <sup>14</sup> C std (±)	fraction	E (kJ/mol)	E std. (± kJ/mol)
Fm3_AL2	150-240	1566	2702	106.600	2.698	0.337	0.005	1	121	6
Fm3_AL2	240-300	2703	3614	231.053	5.849	0.339	0.007	2	133	7
Fm3_AL2	300-350	3615	4367	188.344	4.768	0.324	0.006	3	145	7
Fm3_AL2	350-400	4368	5135	144.903	3.668	0.329	0.006	4	159	9
Fm3_AL2	400-455	5136	5966	203.368	5.148	0.341	0.005	5	171	6
Fm3_AL2	455-510	5967	6819	113.911	2.883	0.328	0.005	6	179	6
Fm3_AL2	510-600	6820	8255	26.235	0.664	0.327	0.006	7	193	6
Fm3_AL2	600-900	NA	NA	0.000	0.000	NA	NA	8	0	0
Fm3_AL3	150-240	1485	2625	43.726	1.107	0.309	0.006	1	122	7
Fm3_AL3	240-300	2626	3536	112.809	2.856	0.294	0.005	2	133	7
Fm3_AL3	300-350	3537	4291	101.437	2.568	0.268	0.005	3	145	7
Fm3_AL3	350-400	4292	5056	85.077	2.154	0.295	0.005	4	158	8
Fm3_AL3	400-455	5057	5897	90.473	2.290	0.271	0.005	5	171	7
Fm3_AL3	455-510	5898	6739	61.264	1.551	0.272	0.005	6	182	7
Fm3_AL3	510-600	6740	8055	32.785	0.830	0.267	0.007	7	197	8
Fm3_AL3	600-900	8056	9690	7.877	0.199	NA	NA	8	222	10
Fm3_HO	150-240	1714	2840	5.925	0.150	0.106	0.004	1	129	6
Fm3_HO	240-300	2841	3763	49.912	1.263	0.074	0.003	2	136	7
Fm3_HO	300-350	3764	4513	87.868	2.224	0.049	0.002	3	147	7
Fm3_HO	350-400	4514	5267	112.679	2.852	0.038	0.002	4	158	7
Fm3_HO	400-455	5268	6111	108.595	2.749	0.031	0.002	5	170	8
Fm3_HO	455-510	6112	6958	92.931	2.352	0.017	0.002	6	185	8
Fm3_HO	510-600	6959	8341	100.007	2.531	0.023	0.002	7	199	8
Fm3_HO	600-900	8342	10665	26.833	0.679	NA	NA	8	223	13
Fm3_DB	150-240	1558	2703	4.864	0.123	0.133	0.004	1	130	6
Fm3_DB	240-300	2704	3595	43.497	1.101	0.084	0.003	2	136	7
Fm3_DB	300-350	3596	4356	82.889	2.098	0.050	0.002	3	147	7
Fm3_DB	350-400	4357	5119	105.309	2.666	0.038	0.002	4	158	7
Fm3_DB	400-455	5120	5957	94.050	2.381	0.028	0.002	5	170	8
Fm3_DB	455-510	5958	6806	80.504	2.038	0.024	0.002	6	185	8
Fm3_DB	510-600	6807	8193	77.433	1.960	0.025	0.002	7	198	8
Fm3_DB	600-900	8194	10508	13.925	0.352	NA	NA	8	218	11
Fm3_RU	150-240	1424	2564	15.129	0.383	0.116	0.003	1	126	6
Fm3_RU	240-300	2565	3481	82.297	2.083	0.071	0.003	2	135	7
Fm3_RU	300-350	3482	4241	128.834	3.261	0.050	0.003	3	147	7
Fm3_RU	350-400	4242	4987	137.515	3.481	0.043	0.002	4	157	7
Fm3_RU	400-455	4988	5833	112.279	2.842	0.043	0.002	5	171	8
Fm3_RU	455-510	5834	6677	98.011	2.481	0.042	0.002	6	183	7
Fm3_RU	510-600	6678	8065	65.172	1.650	0.041	0.002	7	197	8
Fm3_RU	600-900	8066	10379	7.000	0.177	NA	NA	8	215	11

**Table S4.** Summary of identified peaks from Py–GCMS analyses across thermal windows (150–850 °C) for Fm2 and Fm3 samples. See separate file PyroGCMS\_Fm2\_Fm3\_150\_850.csv. Columns include Source File, Sample, Peak Number, Retention Time, Peak Area, Peak Area [%], Target (OpenChrom identification), and Classifier (compound group).

Supplementary figures

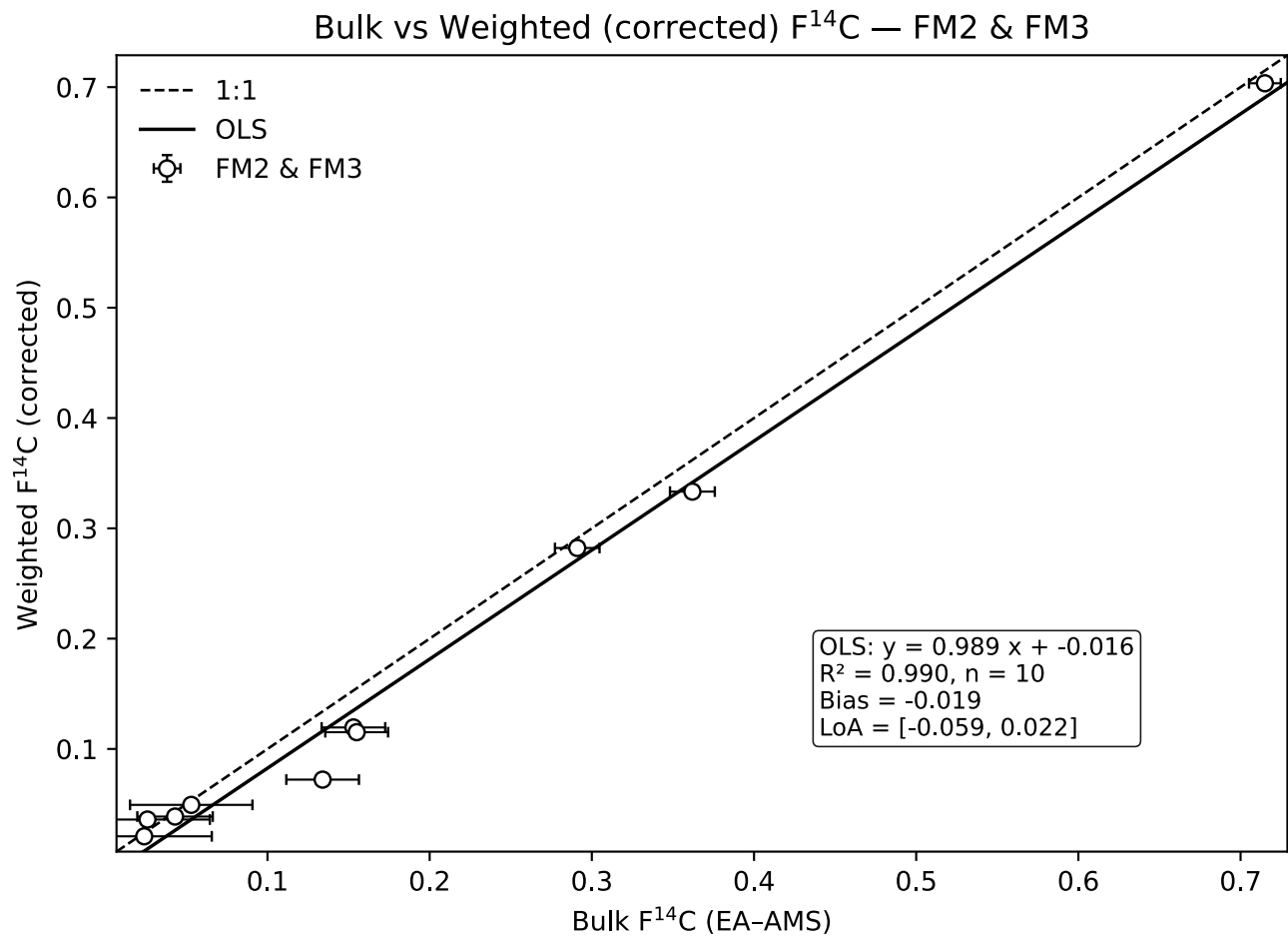


**Figure S1.** Comparison between thermally integrated (weighted) and bulk F<sup>14</sup>C values for thaw-slump samples from FM2 and FM3 both in circles Bulk F<sup>14</sup>C were taken from Bröder et al. (2021). The 1:1 line (grey dashed) marks perfect agreement. Weighted values closely reproduce bulk F<sup>14</sup>C measurements (OLS = 0.989 x – 0.016; R<sup>2</sup> = 0.99), confirming that the thermal integration approach captures the bulk radiocarbon signal within analytical uncertainty.

Comparison of ROC/TOC ratios derived from SoliTOC and ORO–AMS reveals consistent trends across geomorphic features, validating the use of this metric for assessing OM thermal stability. In both datasets, PF, DB, and RU samples exhibit moderate

45 to high ROC/TOC values, indicating a dominance of thermally resistant carbon in remobilised and permafrost compartments. In contrast, AL samples — especially from FM2 — display lower ROC/TOC ratios (e.g., 0.24 for SoliTOC and 0.12 for ORO–AMS), reflecting greater contributions from labile and biologically active OM. While absolute values differ, typically with ORO–AMS reporting slightly lower ROC/TOC ratios, the relative order remains consistent across sites. The difference arises because ORO–AMS resolves oxidation continuously across the thermal spectrum, whereas SoliTOC defines discrete  
50 temperature intervals. This finer resolution leads to what was previously described as “more granular thermal fractionation,” meaning that ORO–AMS captures partial oxidation within the 400 °C boundary rather than assigning all remaining carbon above this point to the ROC fraction.

The coherence between these two independent methods therefore primarily demonstrates analytical comparability — that carbon oxidised below 400 °C in one system tends to do so in the other — rather than implying direct geomorphic control.

55

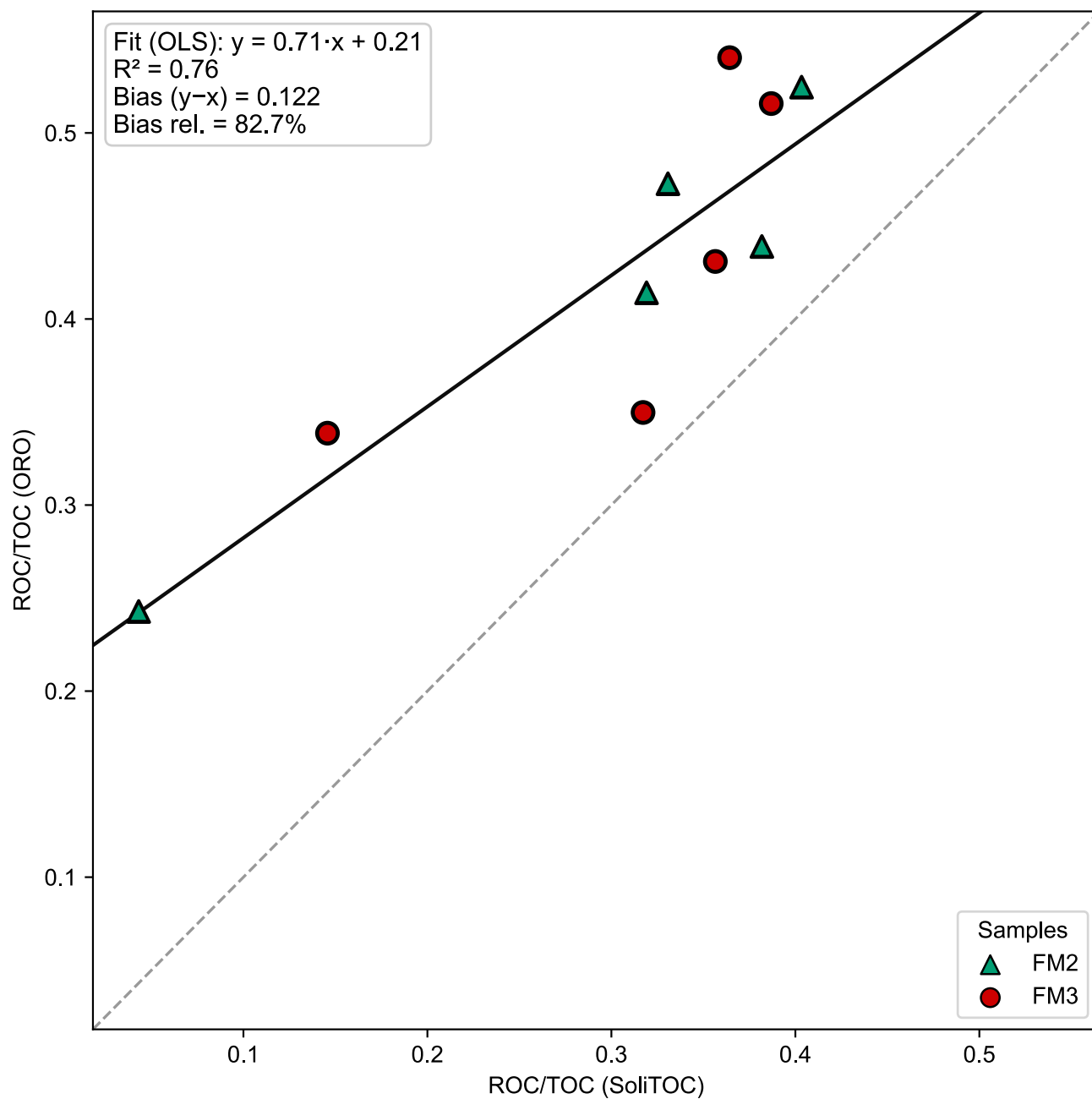


**Figure S2.** Cross-plot comparison of ROC/TOC ratios obtained from SoliTOC and ORO–AMS analyses for thaw-slump samples from FM2 (green triangles) and FM3 (red circles). The 1:1 line (grey dashed) indicates perfect agreement. A consistent offset is observed, with ORO–AMS reporting systematically higher ROC/TOC values (slope = 0.71,  $R^2 = 0.76$ , bias  $\approx 0.12$ ), reflecting methodological differences between continuous and stepped combustion.

However, when interpreted together with thermogram and molecular data, the pattern still supports a geomorphic gradient in OM reactivity: thermally stable carbon accumulates in PF, DB, and RU, while the AL retains fresher, more reactive OM influenced by vegetation cover, thaw depth, and cryogenic disturbance. Differences in absolute ROC/TOC ratios between  
65 SoliTOC and ORO–AMS are largely methodological. The continuous ramping approach of ORO–AMS and the discrete temperature steps of SoliTOC partition intermediate thermal fractions differently, leading to systematic offsets in ROC/TOC values. In particular, intermediate-temperature carbon fractions may be assigned differently between methods, resulting in higher apparent ROC/TOC values in ORO–AMS compared to SoliTOC. This offset ( $\sim 0.2$  on average in our dataset) is consistent with inter-method differences reported in similar comparative studies. These method-inherent biases highlight the  
70 value of using multiple thermal approaches to constrain OM reactivity and underscore the complementarity of SoliTOC and ORO–AMS.

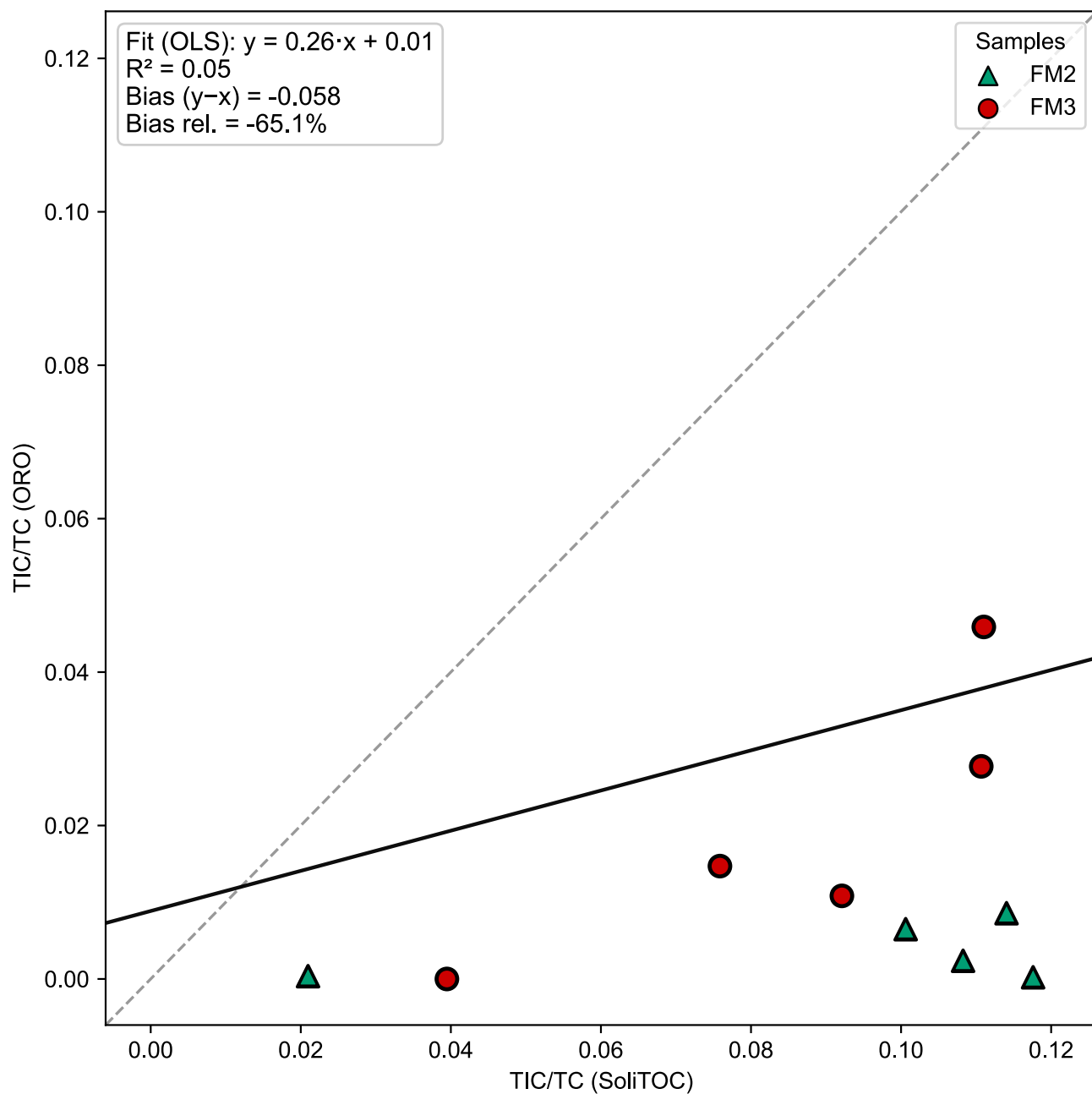
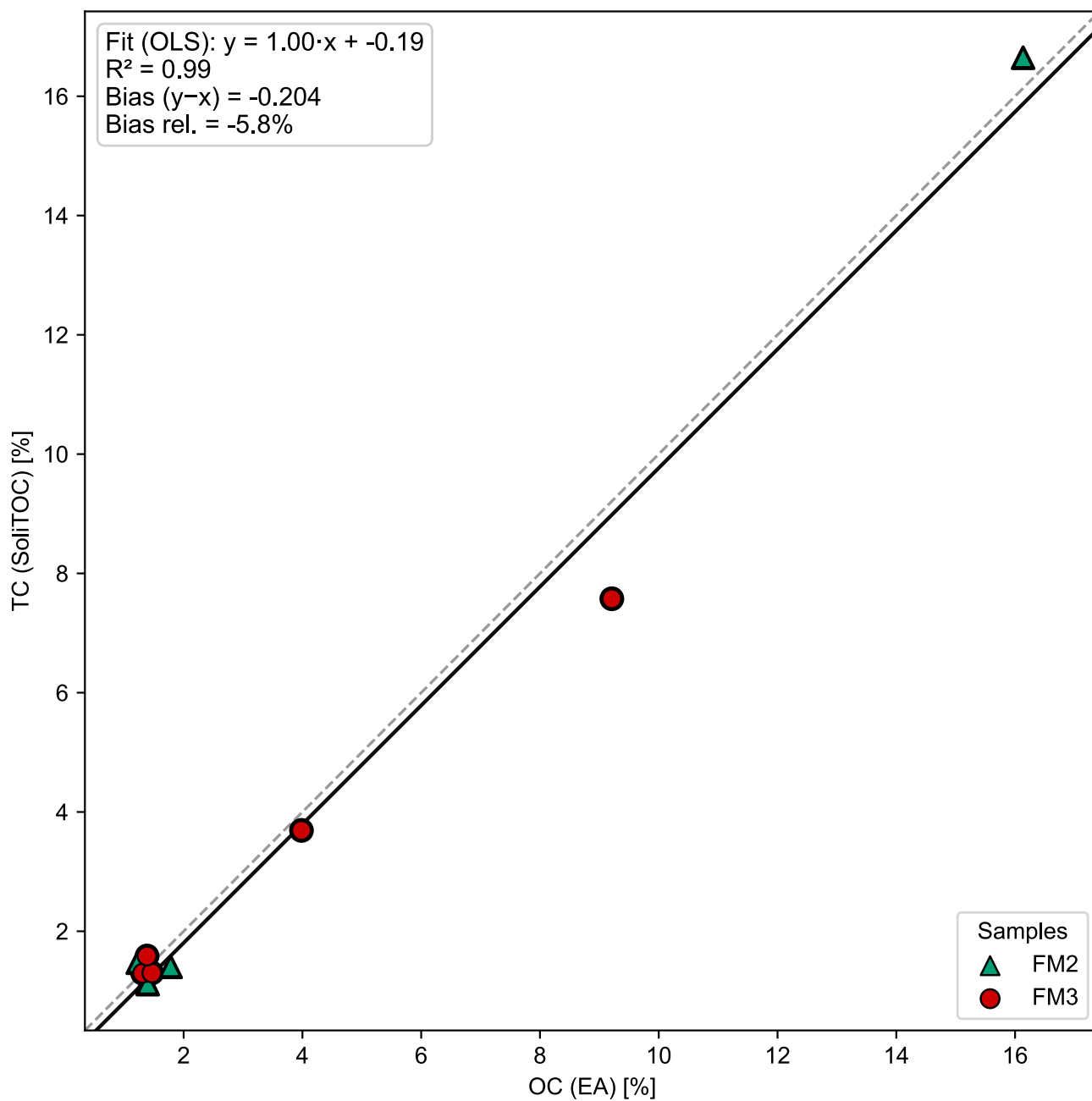


**Figure S3.** Cross-plot comparison of TIC/TC ratios obtained from SoliTOC and ORO analyses for thaw-slump samples from FM2 (green triangles) and FM3 (red circles). The 1:1 line (grey dashed) marks perfect agreement. Values show large scatter and no systematic 1:1 relationship (slope = 0.26,  $R^2 = 0.05$ , bias  $\approx -65.1$ ), indicating that TIC/TC is highly method-dependent. This reflects the very small carbon fraction oxidised  $>900$  °C and differences in operational temperature windows, integration procedures, and instrument sensitivity between SoliTOC and ORO.

80 The two metrics show poor agreement and substantial scatter relative to the 1:1 line, with a systematic tendency for ORO to  
yield lower TIC/TC values than SoliTOC. This directional bias reflects fundamental differences in how carbonate  
decomposition is achieved by the two instruments. SoliTOC relies on fixed isothermal holds between 600 and 900 °C, during  
which some high-temperature carbonates (e.g. Mg-rich or Fe-bearing phases) may not fully decompose, leading to  
underestimation of TIC. In contrast, ORO applies continuous high-temperature oxidation under pure O<sub>2</sub>, which more  
85 completely decomposes residual carbonates and produces larger TIC signals.

Superimposed on this directional offset is substantial scatter. Because TIC represents <1 % of total carbon after acidification,  
small variations in CO<sub>2</sub> yield, baseline subtraction, or signal integration translate into large relative differences when expressed  
as TIC/TC. The ORO detection chain is also more sensitive to minor adsorption, leaks, or memory effects than SoliTOC's  
90 direct TGA–IR configuration, further amplifying variability in this tail fraction. Together, these effects demonstrate that  
TIC/TC is strongly method-dependent and unsuitable for quantitative cross-method comparison.

By comparison, total organic carbon (TOC) measured by SoliTOC closely matches independently measured OC from  
elemental analysis (EA) (Fig. S4;  $R^2 = 0.99$ , slope = 1.00), confirming robust bulk carbon quantification. Total carbon estimates  
95 derived from ORO–AMS are also comparable to EA-OC values (Table S3), although agreement is less systematic because  
ORO-based values rely on mg-precision mass determination rather than direct carbon quantification. Consequently, inter-  
method interpretation is restricted to the more robust operational fractions (TOC<sub>400</sub> and ROC), which show consistent  
behaviour across techniques.



100 **Figure S4.** Cross-plot comparison of TC measured by SoliTOC and OC measured by elemental analysis (EA) for thaw-slump samples (Bröder et al., 2021) from FM2 (green triangles) and FM3 (red circles). The 1:1 line (grey dashed) indicates perfect agreement. TC and OC(EA) show near-identical values across samples (slope = 1.00,  $R^2 = 0.99$ , bias  $\approx -0.20$ ), confirming that

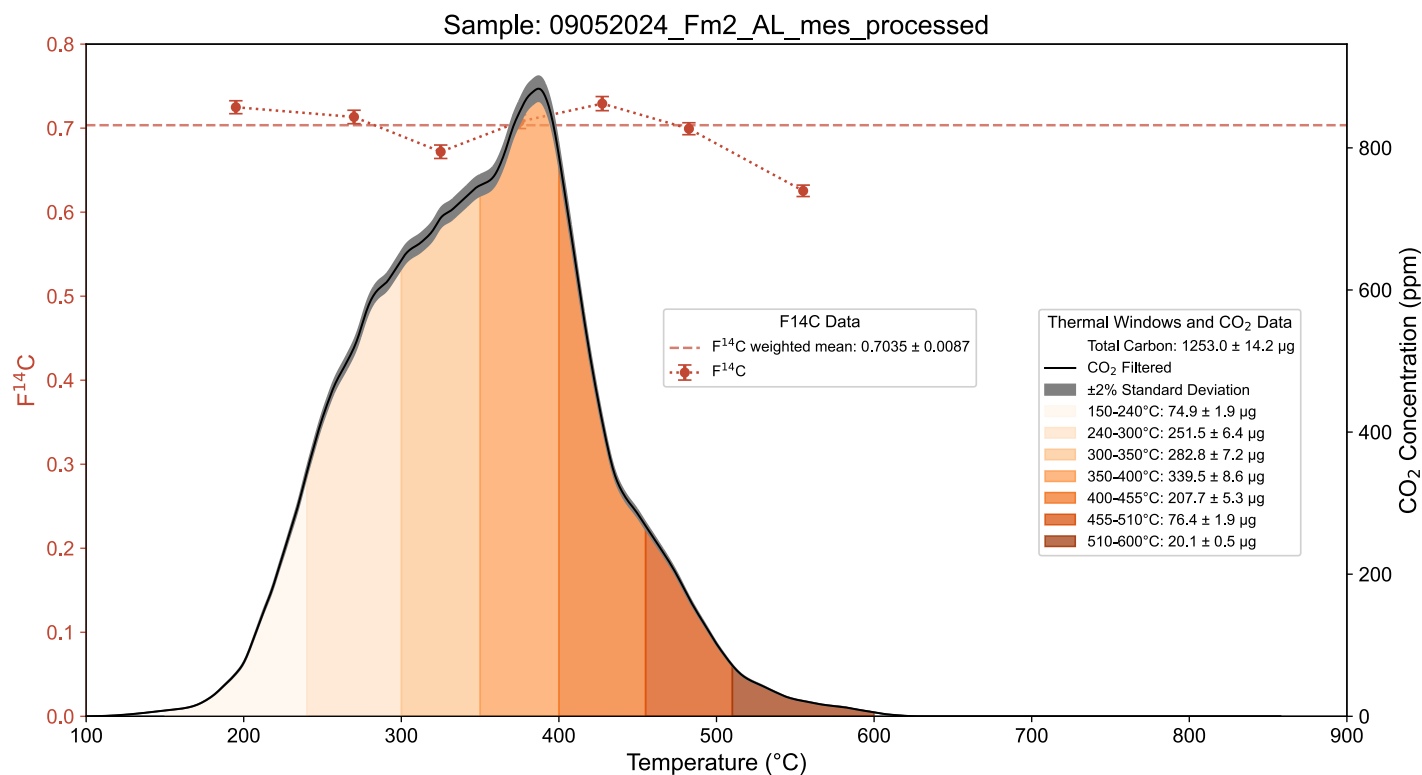


SoliTOC-derived total carbon closely matches independent EA-OC measurements after acidification and indicating robust quantification of the bulk organic carbon pool.

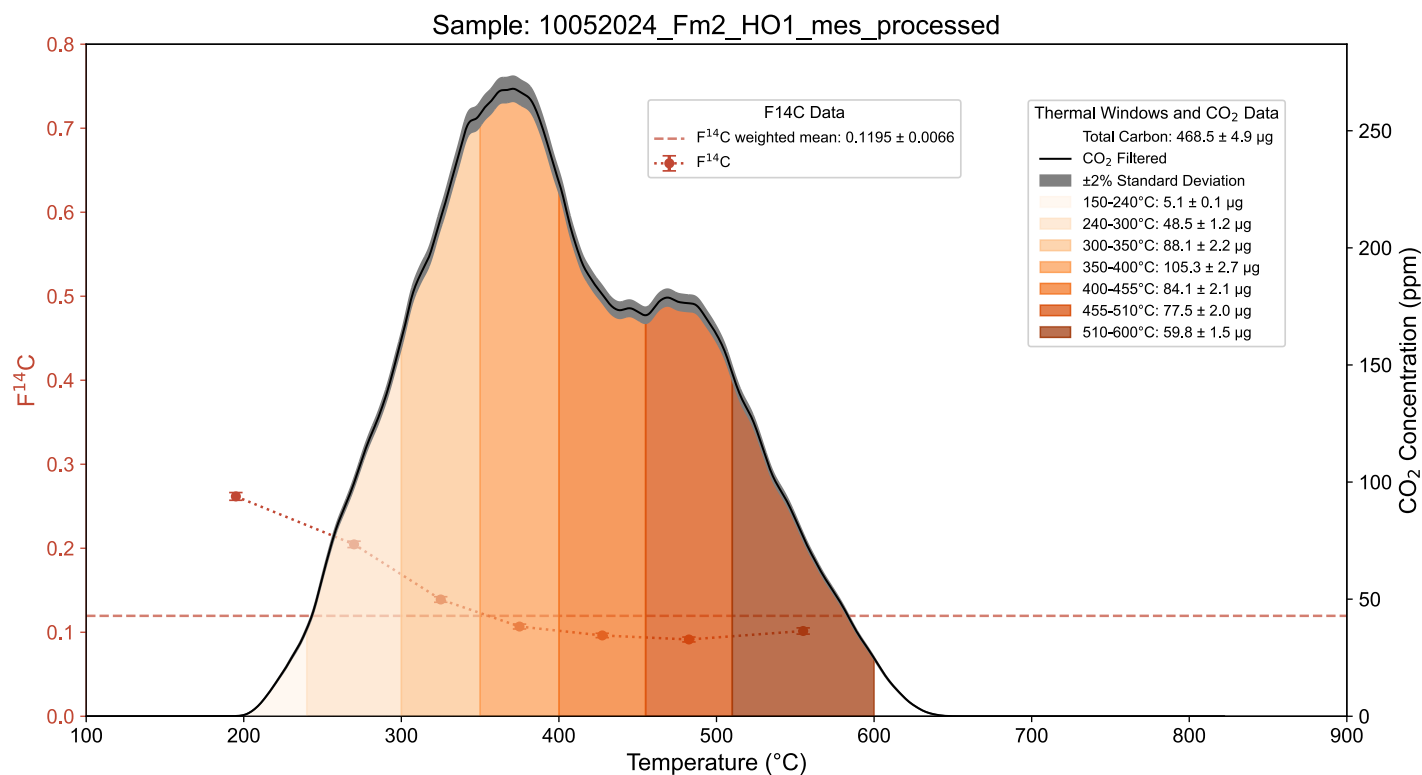
105

To verify the consistency of total organic carbon quantification across independent analytical methods, we compared TC values from SoliTOC with OC measurements obtained via elemental analysis (EA). All samples were acidified prior to both analyses, ensuring that measured carbon corresponds to organic carbon. The cross-plot (Fig. S4) shows excellent agreement between the two methods, with all samples falling close to the 1:1 line and a regression slope of  $\sim 1.00$  ( $R^2 = 0.99$ ). The small absolute bias ( $\approx -0.20$  %) indicates slightly lower TC values from SoliTOC relative to EA, but the deviation is within expected analytical uncertainty for low-mass permafrost samples. This strong correspondence demonstrates that SoliTOC reliably quantifies bulk organic carbon, and that downstream ratios ( $\text{TOC}_{400}/\text{TOC}$ ,  $\text{ROC}/\text{TOC}$ ) are not affected by methodological inconsistencies in total-carbon estimation.

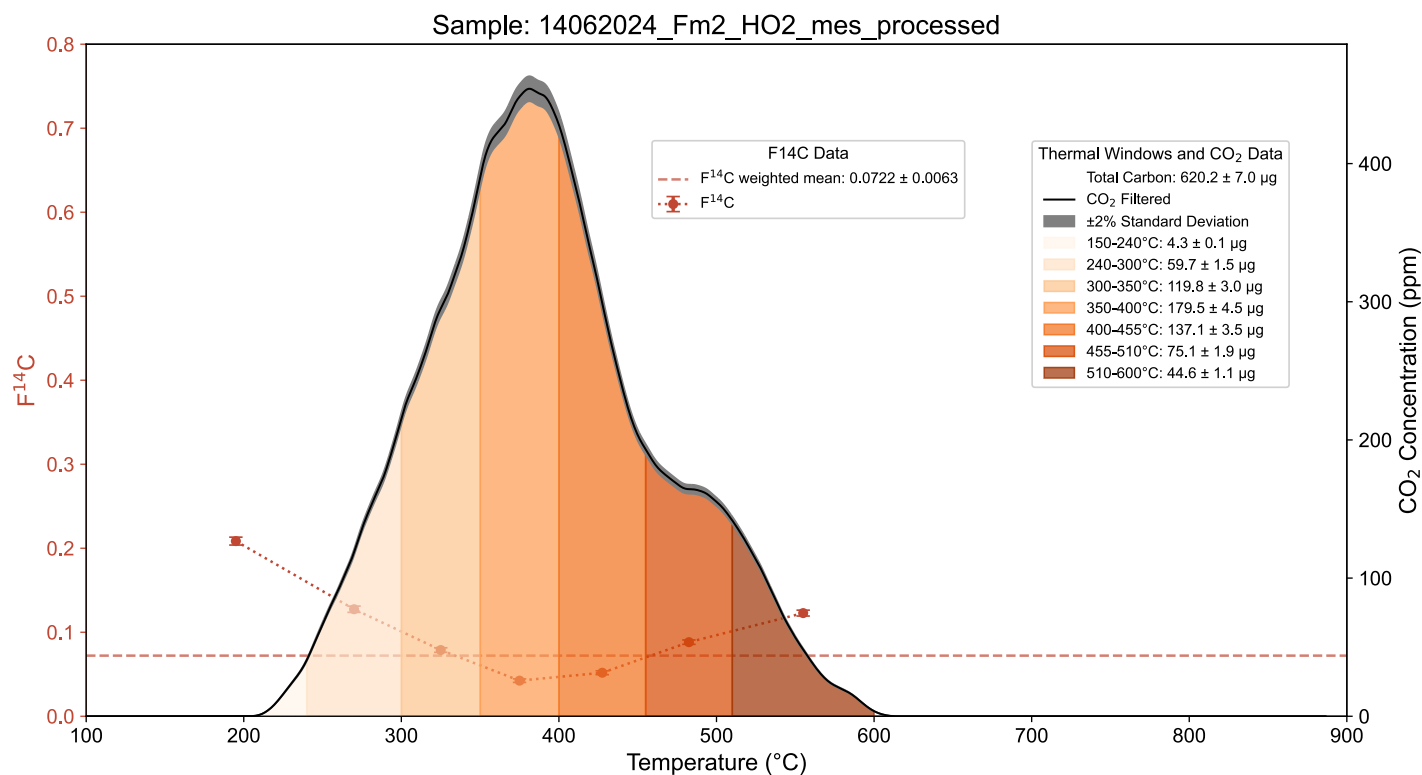
110



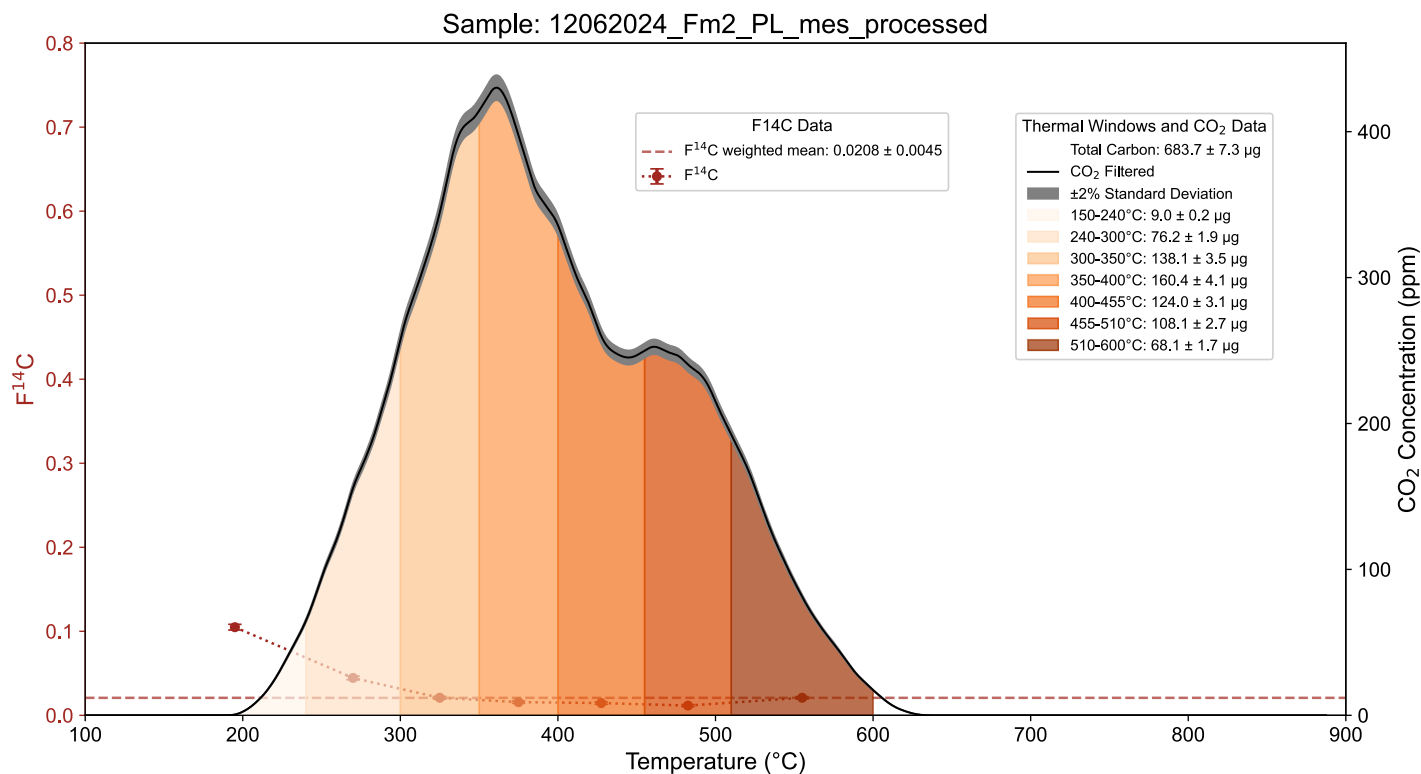
**Figures S5.** Thermogram of FM2-AL shows CO<sub>2</sub> release as a function of temperature for each sample, overlaid with corresponding F<sup>14</sup>C values across defined thermal windows. For each thermal window, the legends show the calculated carbon mass released (with associated error), the mass fraction (%), and the weighted F<sup>14</sup>C (with standard deviation). These data illustrate the relationship between carbon release dynamics, radiocarbon content, and the distribution of mass across the thermal profile.



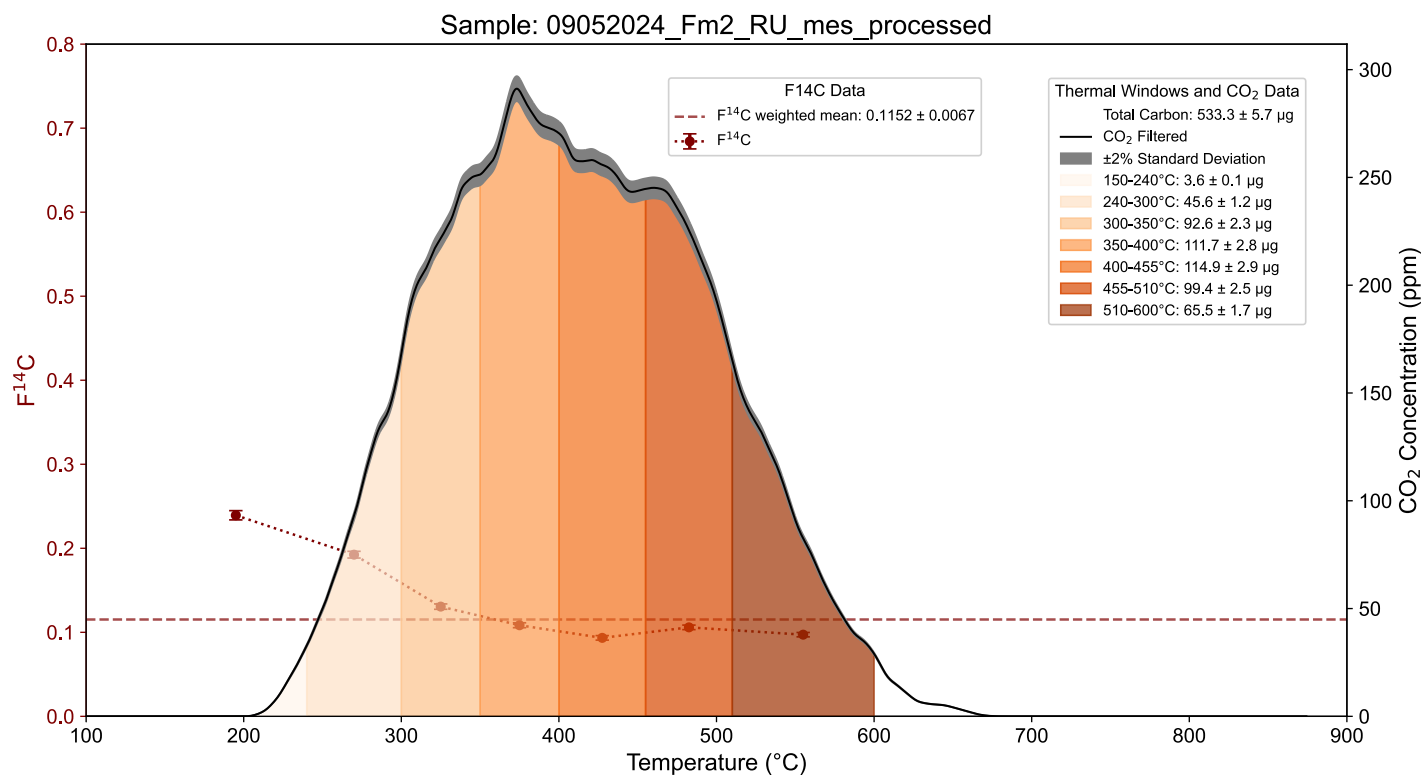
**Figures S6.** Thermogram of FM2-HO1 shows CO<sub>2</sub> release as a function of temperature for each sample, overlaid with corresponding F<sup>14</sup>C values across defined thermal windows. For each thermal window, the legends show the calculated carbon mass released (with associated error), the mass fraction (%), and the weighted F<sup>14</sup>C (with standard deviation). These data illustrate the relationship between carbon release dynamics, radiocarbon content, and the distribution of mass across the thermal profile.



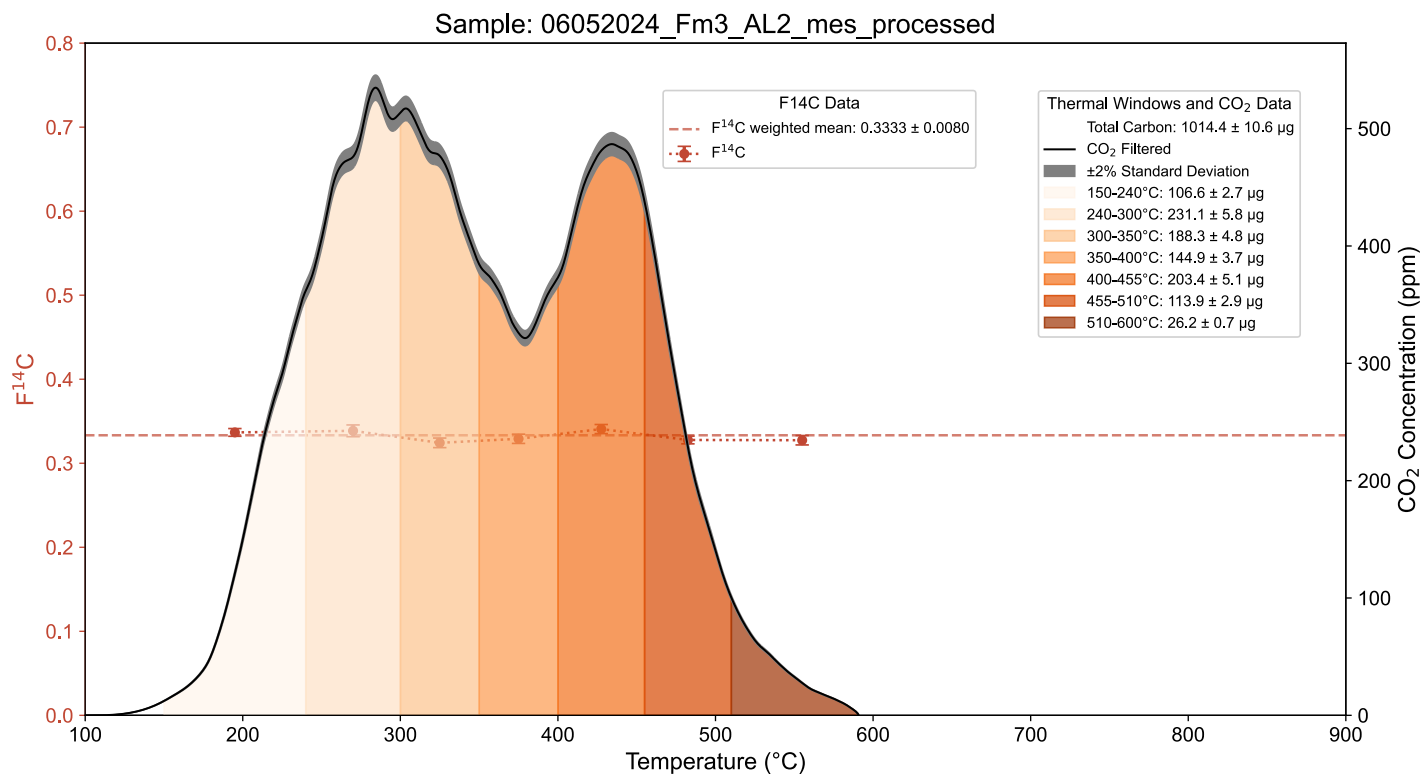
**Figures S7.** Thermogram of FM2-HO2 shows CO<sub>2</sub> release as a function of temperature for each sample, overlaid with corresponding F<sup>14</sup>C values across defined thermal windows. For each thermal window, the legends show the calculated carbon mass released (with associated error), the mass fraction (%), and the weighted F<sup>14</sup>C (with standard deviation). These data illustrate the relationship between carbon release dynamics, radiocarbon content, and the distribution of mass across the thermal profile.



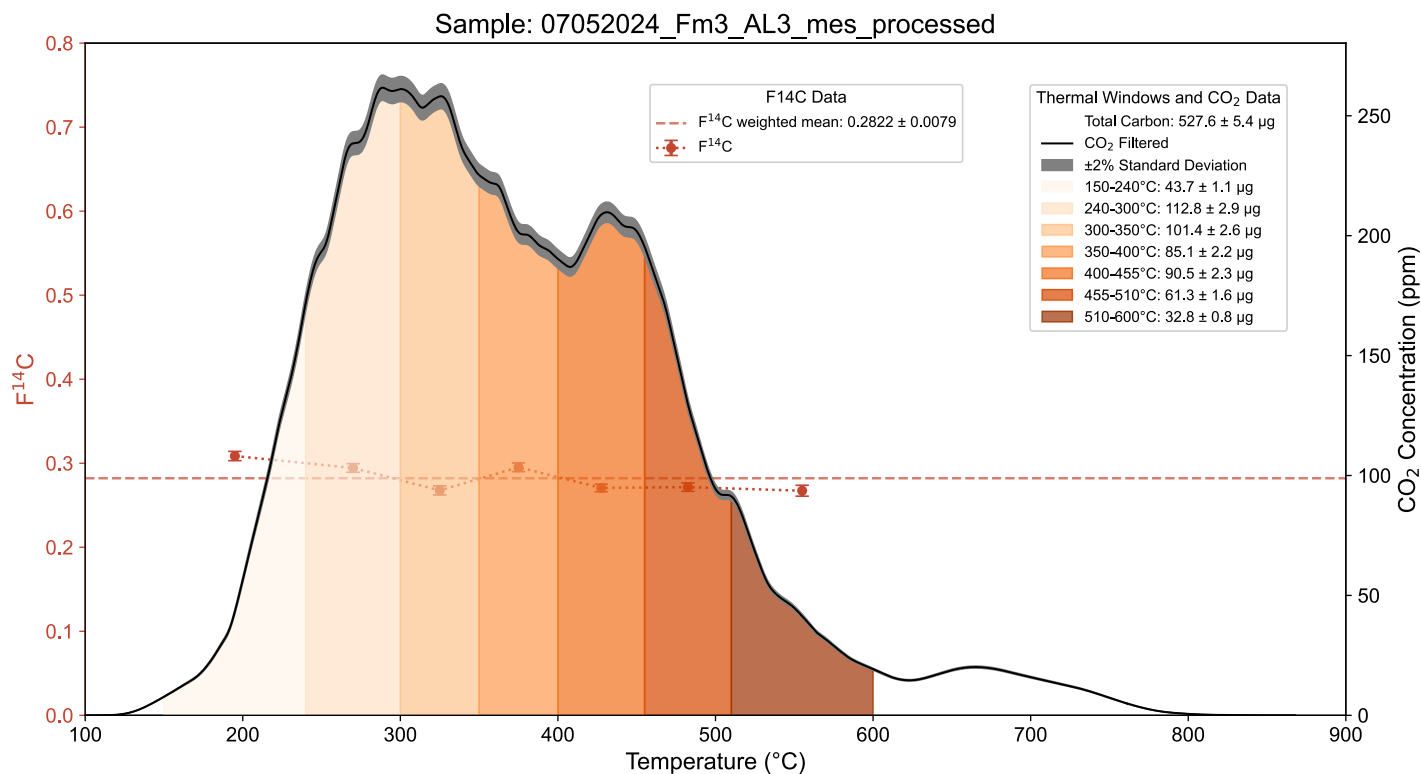
**Figures S8.** Thermogram of FM2-PL shows CO<sub>2</sub> release as a function of temperature for each sample, overlaid with corresponding F<sup>14</sup>C values across defined thermal windows. For each thermal window, the legends show the calculated carbon mass released (with associated error), the mass fraction (%), and the weighted F<sup>14</sup>C (with standard deviation). These data illustrate the relationship between carbon release dynamics, radiocarbon content, and the distribution of mass across the thermal profile.



130 **Figures S9.** Thermogram of FM2-RU shows CO<sub>2</sub> release as a function of temperature for each sample, overlaid with corresponding F<sup>14</sup>C values across defined thermal windows. For each thermal window, the legends show the calculated carbon mass released (with associated error), the mass fraction (%), and the weighted F<sup>14</sup>C (with standard deviation). These data illustrate the relationship between carbon release dynamics, radiocarbon content, and the distribution of mass across the thermal profile.

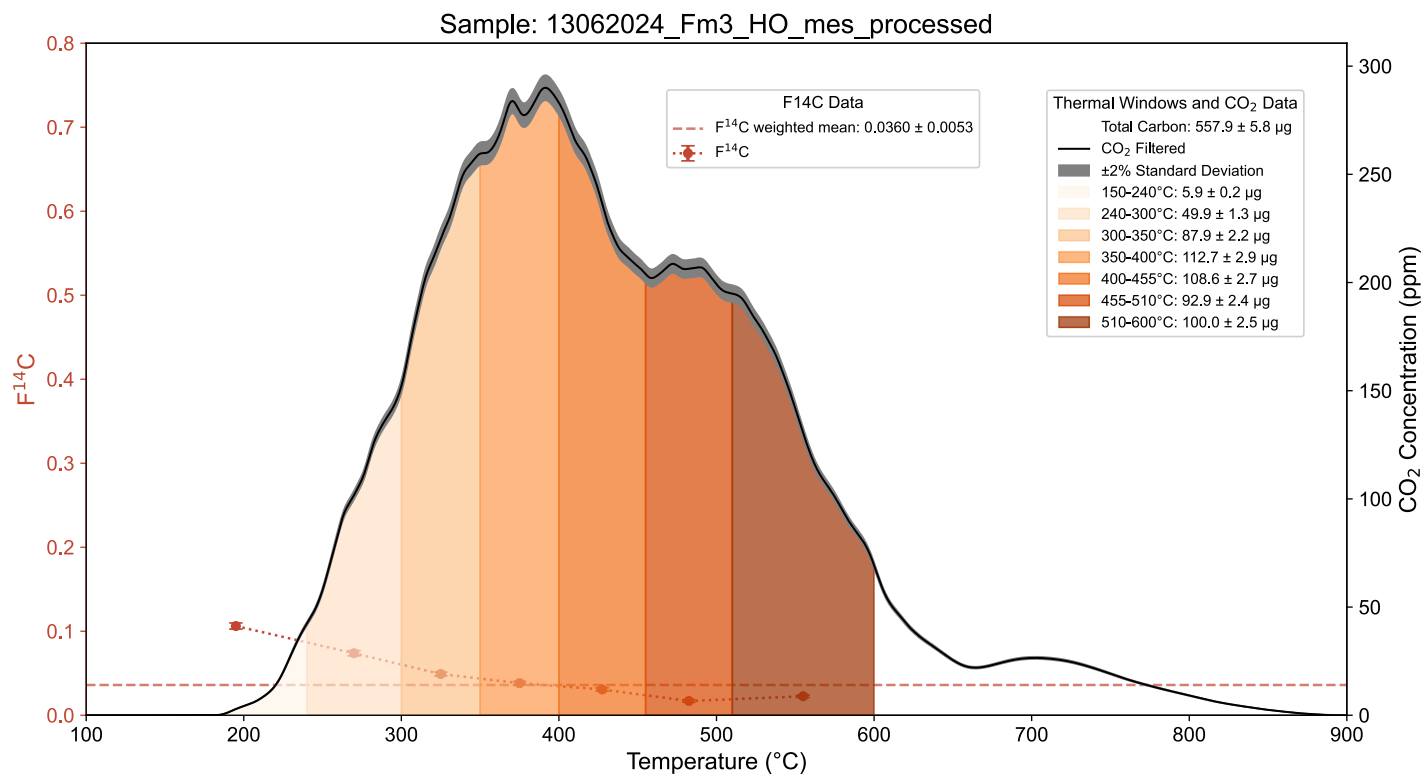


**Figures S10.** Thermogram of FM3-AL2 shows CO<sub>2</sub> release as a function of temperature for each sample, overlaid with corresponding F<sup>14</sup>C values across defined thermal windows. For each thermal window, the legends show the calculated carbon mass released (with associated error), the mass fraction (%), and the weighted F<sup>14</sup>C (with standard deviation). These data illustrate the relationship between carbon release dynamics, radiocarbon content, and the distribution of mass across the thermal profile.

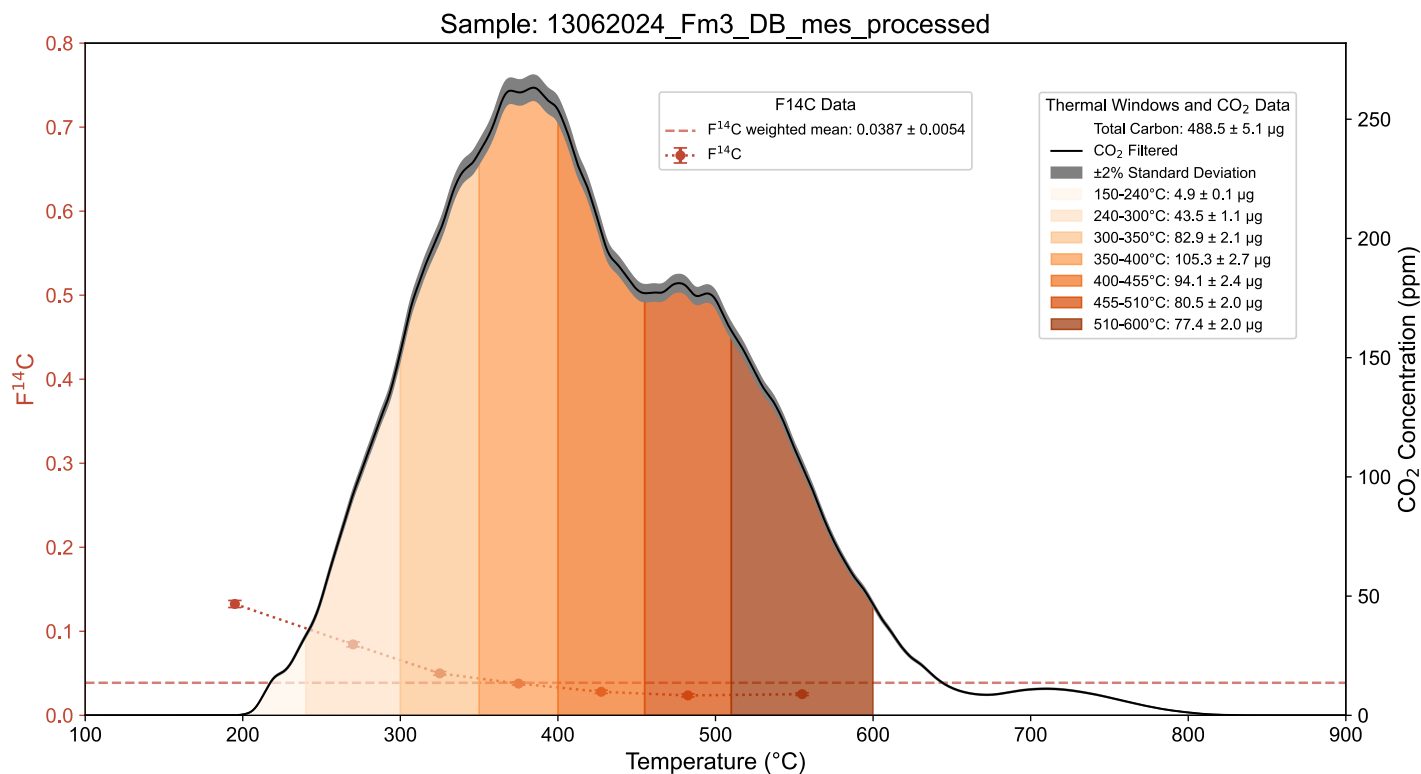


**Figures S11.** Thermogram of FM3-AL3 shows CO<sub>2</sub> release as a function of temperature for each sample, overlaid with corresponding F<sup>14</sup>C values across defined thermal windows. For each thermal window, the legends show the calculated carbon mass released (with associated error), the mass fraction (%), and the weighted F<sup>14</sup>C (with standard deviation). These data illustrate the relationship between carbon release dynamics, radiocarbon content, and the distribution of mass across the thermal profile.

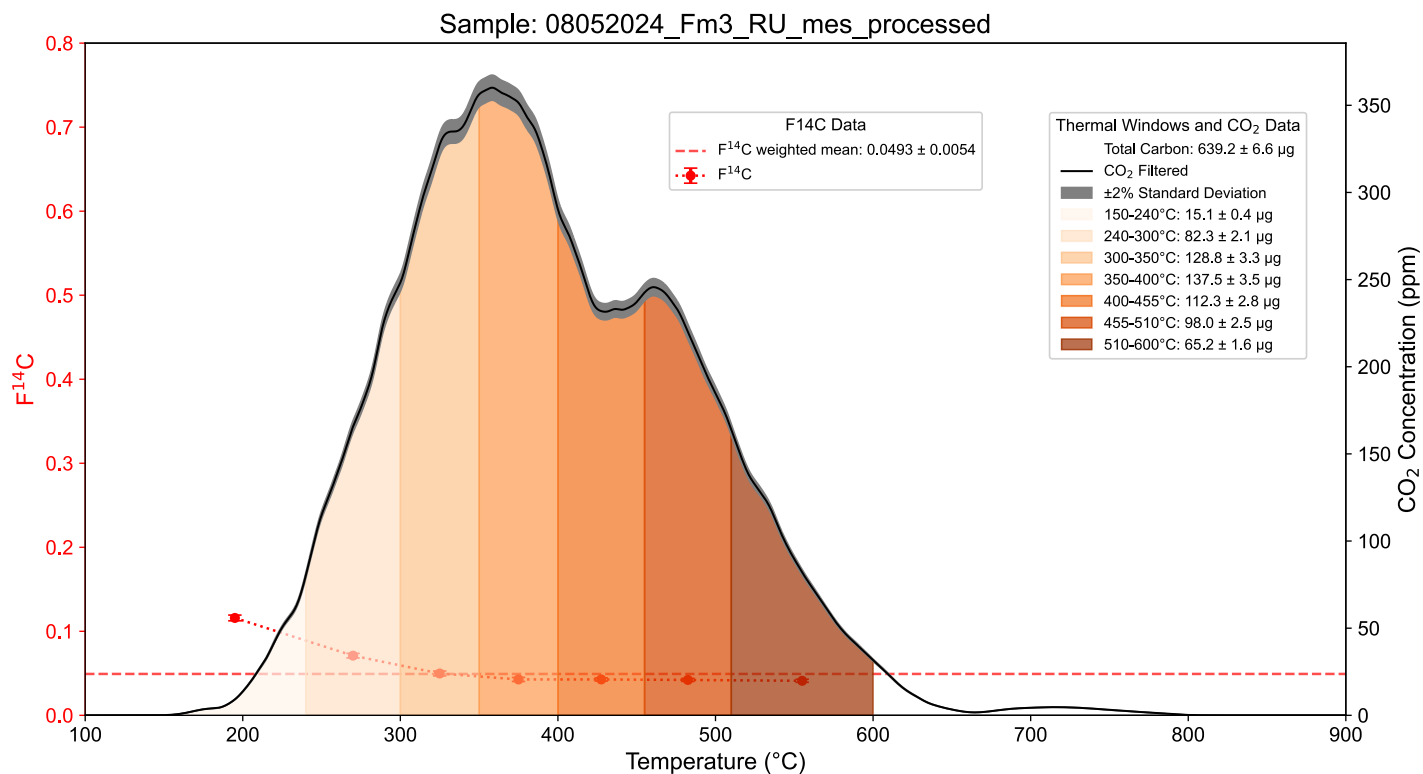




**Figures S12.** Thermogram of FM3-HO shows CO<sub>2</sub> release as a function of temperature for each sample, overlaid with corresponding F<sup>14</sup>C values across defined thermal windows. For each thermal window, the legends show the calculated carbon mass released (with associated error), the mass fraction (%), and the weighted F<sup>14</sup>C (with standard deviation). These data illustrate the relationship between carbon release dynamics, radiocarbon content, and the distribution of mass across the thermal profile.



**Figures S13.** Thermogram of FM3-DB shows CO<sub>2</sub> release as a function of temperature for each sample, overlaid with corresponding F<sup>14</sup>C values across defined thermal windows. For each thermal window, the legends show the calculated carbon mass released (with associated error), the mass fraction (%), and the weighted F<sup>14</sup>C (with standard deviation). These data illustrate the relationship between carbon release dynamics, radiocarbon content, and the distribution of mass across the thermal profile.



150 **Figures S14.** Thermogram of FM3-RU shows CO<sub>2</sub> release as a function of temperature for each sample, overlaid with corresponding F<sup>14</sup>C values across defined thermal windows. For each thermal window, the legends show the calculated carbon mass released (with associated error), the mass fraction (%), and the weighted F<sup>14</sup>C (with standard deviation). These data illustrate the relationship between carbon release dynamics, radiocarbon content, and the distribution of mass across the thermal profile.

# Compound-class proportions (stacked) with $F^{14}C$ (points) by sample type

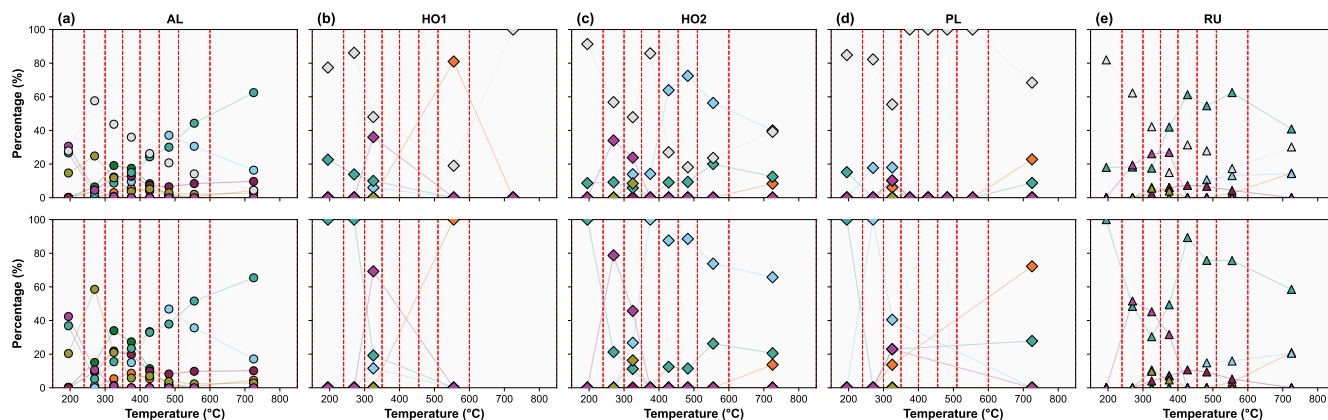
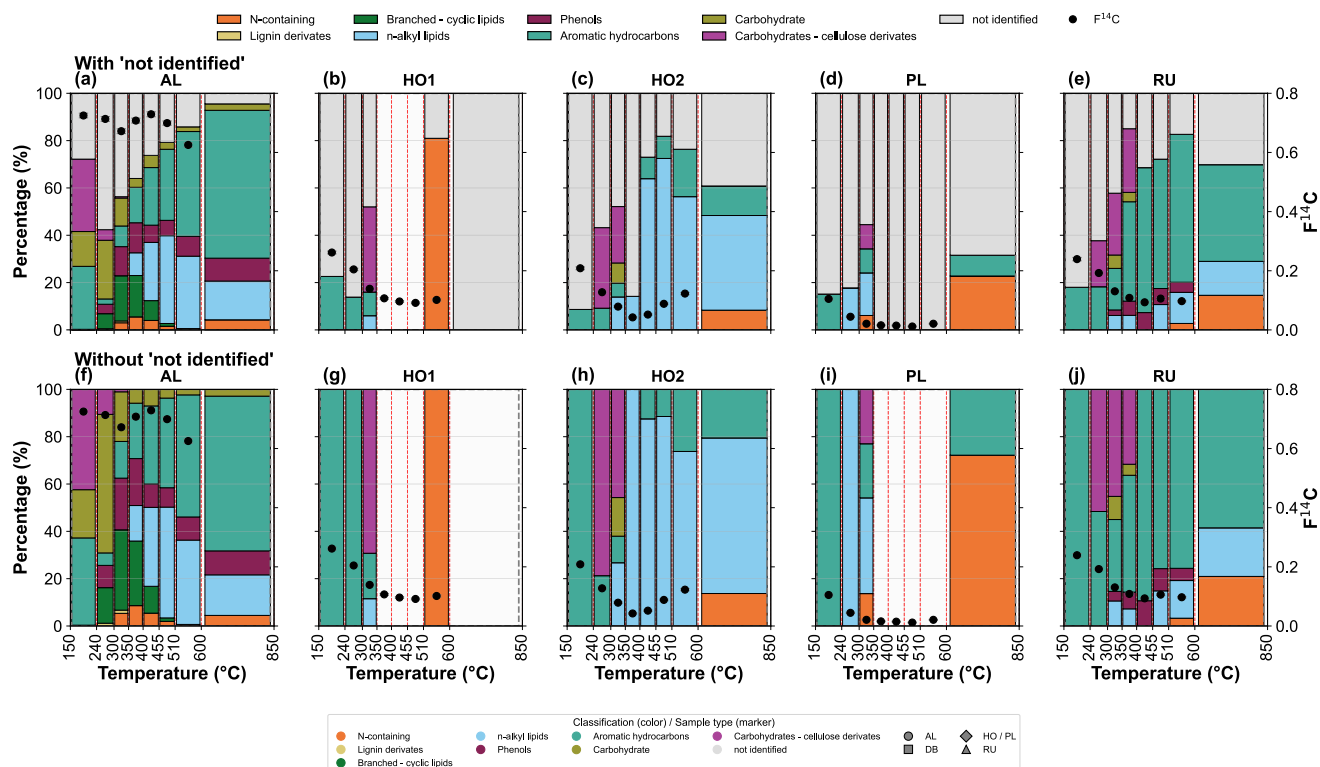


**Figure S15.** Normalised Ts-Py-GCMS peak-area distributions across thermal windows (150–850 °C) for Fm2 features.

Top two rows (a–j): stacked plots showing compound-class distributions across thermal windows. Each feature is represented by paired panels — top includes all compounds; bottom excludes “not identified” compounds to emphasise major classes (N-containing, lignin derivatives, branched/cyclic lipids, n-alkyl lipids, phenols, aromatic hydrocarbons, carbohydrates, and cellulose derivatives). Feature–panel mapping: (a, f) active layer (AL); (b, g) Holocene permafrost shallow (HO1); (c, h)

Holocene permafrost deep (HO2); (d, i) Pleistocene layer (PL); (e, j) runoff (RU). Bottom two rows (a–e): scatter plots showing relative contributions of major compound classes versus thermal window for each geomorphic feature, highlighting contrasts in compound release, preservation, and compositional variability across Fm2.

# Compound-class proportions (stacked) with F<sup>14</sup>C (points) by sample type

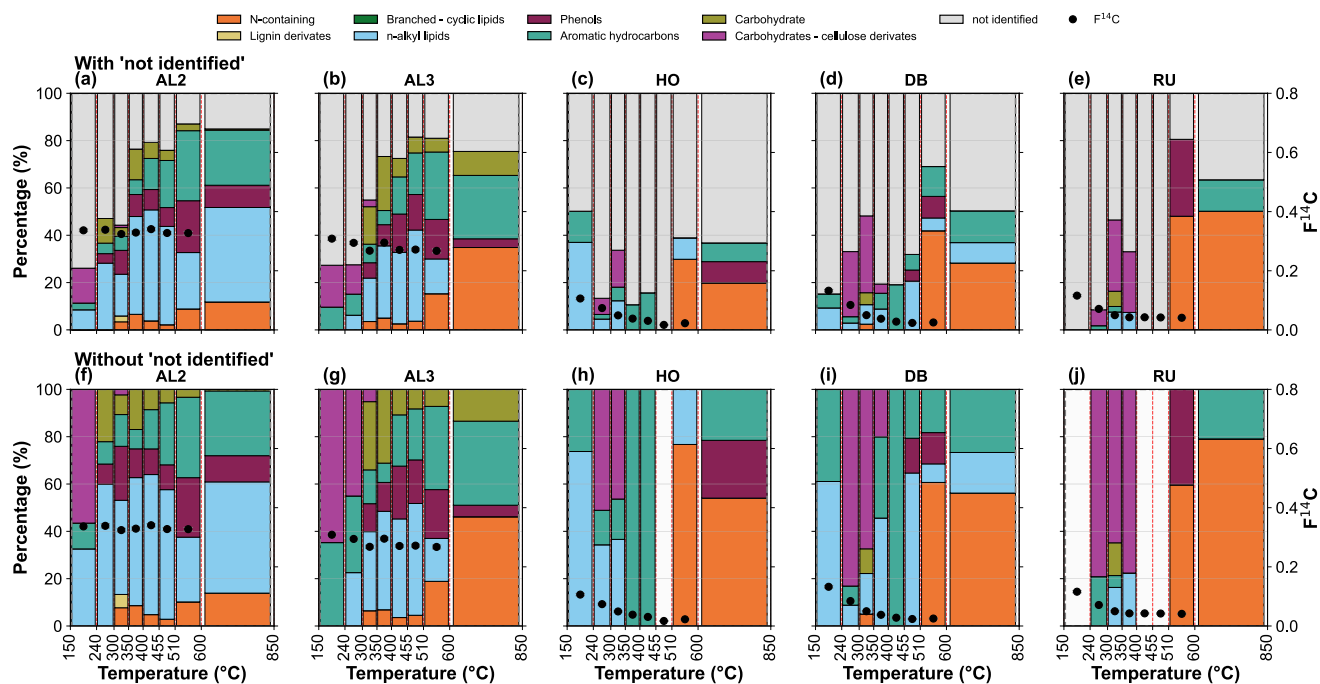


**Figure S16.** Normalised Ts-Py-GCMS peak-area distributions across thermal windows (150–850 °C) for Fm3 features.

Top two rows (a–j): stacked plots showing compound-class distributions across thermal windows. Each feature is represented by paired panels — top includes all compounds; bottom excludes “not identified” compounds to emphasise major classes (N-containing, lignin derivatives, branched/cyclic lipids, n-alkyl lipids, phenols, aromatic hydrocarbons, carbohydrates, and cellulose derivatives). Feature–panel mapping: (a, f) shallow active layer (AL2), (b, g) deep active layer (AL3), (c, h) Holocene

permafrost (HO), (d, i) runoff (RU), (e, j) debris (DB). Bottom two rows (a–e): scatter plots showing relative contributions of major compound classes versus thermal window for each geomorphic feature, highlighting systematic compositional shifts with temperature and pronounced contrasts between shallow and deep active layers.

175

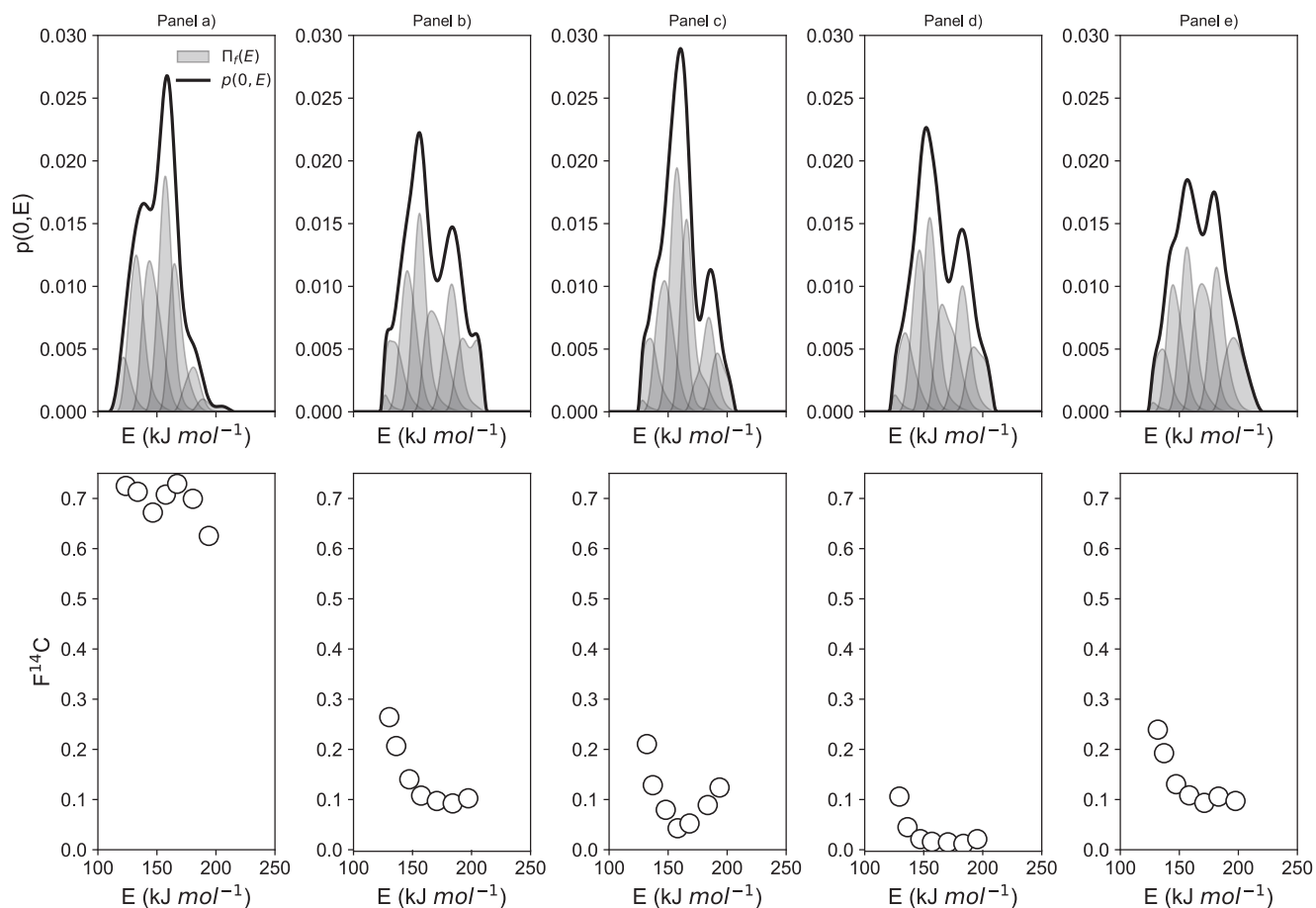


**Figure S17.** Energy distribution of organic matter thermal stability across geomorphic features at the Fm2 sit, following the energy model framework of Hemingway et al. (2019). Panels (a– e) show energy density profiles for: (a) active layer (AL), (b) and (c) Holocene permafrost (HO1, HO2), (d) Pleistocene permafrost (PL), and (e) runoff (RU). The top row displays energy distributions derived from ORO-AMS oxidation steps, while the bottom row overlays corresponding  $F^{14}C$  values on the energy axis. This comparison highlights how carbon age aligns with thermal stability across geomorphic units.



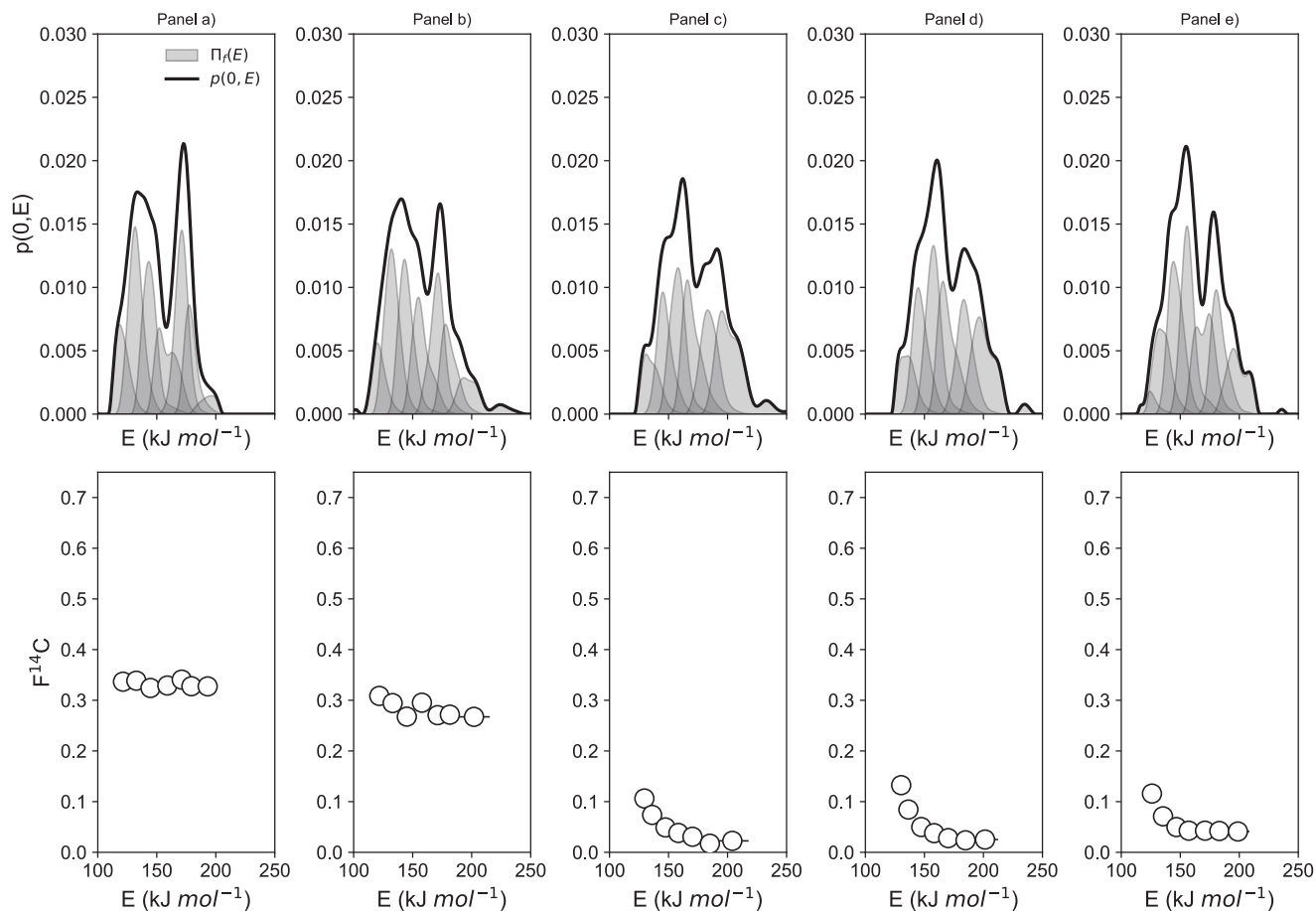


**Figure S18.** Energy distribution of organic matter thermal stability across geomorphic features at the Fm3 site, following the energy model framework of Hemingway et al. (2019). Panels (a)–(e) display the energy density profiles for: (a) active layer 2 (AL2), (b) active layer 3 (AL3), (c) Holocene permafrost (HO), (d) slump debris (DB), and (e) runoff (RU). The upper row presents energy distributions derived from ORO-AMS oxidation windows. The lower row overlays the corresponding  $F^{14}C$  values on the same energy axis, illustrating the relationship between carbon age and energetic stability across compartments.

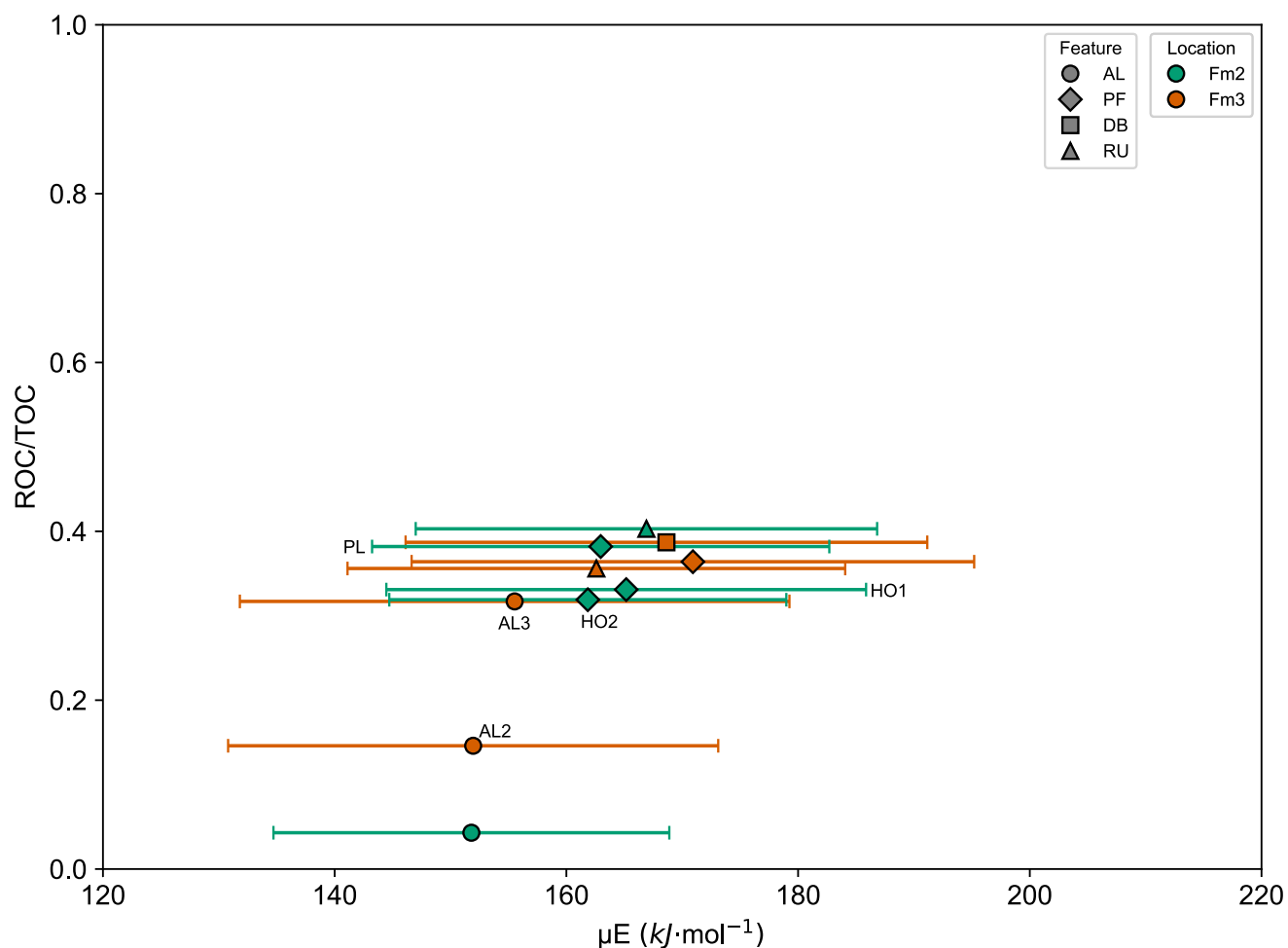


**Figure S19.** Cross-plot comparing the operationally defined recalcitrant-to-total organic carbon ratio (ROC/TOC) from ORO–AMS with mean activation energy ( $\mu E$ ) derived from kinetic modelling. Error bars denote  $\pm\sigma E$ , representing standard deviations of activation-energy distributions. Samples from FM2 (green triangles) and FM3 (red circles) follow a coherent trend in which higher ROC/TOC values generally correspond to higher activation energies, indicating that thermally resistant carbon fractions are associated with more energetically stable material. Variation within each site reflects differences in organic-matter composition across geomorphic units (AL, PF, DB, RU).